Available online at www.sciencedirect.com

SciVerse ScienceDirect

Acta Materialia 61 (2013) 350–359

Acta MATERIALIA

www.elsevier.com/locate/actamat

Direct observation of dislocation dissociation and Suzuki segregation in a Mg–Zn–Y alloy by aberration-corrected scanning transmission electron microscopy

Zhiqing Yang [a,b,c,*], Matthew F. Chisholm [b], Gerd Duscher [c,b], Xiuliang Ma [a], Stephen J. Pennycook [b,c]

[a] Shenyang National Laboratory for Materials Science, Institute of Metal Research, Chinese Academy of Sciences, Shenyang 110016, China
[b] Division of Materials Science and Technology, Oak Ridge National Laboratory, Oak Ridge, TN 37831, USA
[c] Department of Materials Science and Engineering, University of Tennessee, Knoxville, TN 37996, USA

Received 11 July 2012; received in revised form 17 September 2012; accepted 22 September 2012
Available online 17 October 2012

Abstract

Crystal defects in a plastically deformed Mg–Zn–Y alloy have been studied on the atomic scale using aberration-corrected scanning transmission electron microscopy, providing important structural data for understanding the material's deformation behavior and strengthening mechanisms. Atomic scale structures of deformation stacking faults resulting from dissociation of different types of dislocations have been characterized experimentally, and modeled. Suzuki segregation of Zn and Y along stacking faults formed through dislocation dissociation during plastic deformation at 300 °C is confirmed experimentally on the atomic level. The stacking fault energy of the Mg–Zn–Y alloy is evaluated to be in the range of 4.0–10.3 mJ m^{-2}. The newly formed nanometer-wide stacking faults with their Zn/Y segregation in Mg grains play an important role in the superior strength of this alloy at elevated temperatures.

Keywords: Dislocation; Stacking fault; Suzuki segregation; Strength; Mg alloy

1. Introduction

Interactions between dislocations and solute atoms are of long-standing interest, since they have direct influence on the mechanical properties of alloys. Cottrell and Bilby introduced the concept of "atmosphere" in 1949, and successfully explained the plastic deformation and hardening behavior of steels [1]. Soon after, Suzuki [2] pointed out that chemical interactions could induce segregation of solute atoms to stacking faults (SFs). Suzuki segregation is believed to play an important role in the dynamic strain aging of some superalloys [3–6]. Experimental verification of Cottrell atmospheres around dislocations has been achieved with the three-dimensional atom probe [7,8]. However, atomic level experimental identification of Suzuki segregation has not yet been documented, although several electron microscopy investigations have been carried out in order to confirm the Suzuki effect [4,5,9–12]. Kamino et al. [12] reported Si segregation to SFs in a Cu–Si alloy, and depletion of Si on both sides of the SFs in the matrix, based on energy dispersive X-ray spectroscopy (EDS) microanalysis. Han et al. [5] reported Mo and Al enrichment along SFs in a Co–Ni-based superalloy using nano-probe EDS, but no Al/Mo depleted regions were detected beside the SFs. But very recently Koizumi et al. [4] reported that no concentration fluctuation could be detected across SFs in their Co–Ni-based superalloys using EDS and Z-contrast imaging, although phase-field simulation predicted Mo, Cr and Co enrichment along

* Corresponding author at: Shenyang National Laboratory for Materials Science, Institute of Metal Research, Chinese Academy of Sciences, Shenyang 110016, China. Tel.: +86 24 83978275; fax: +86 24 23971215.
E-mail address: yangzq34@yahoo.com (Z. Yang).

1359-6454/$36.00
http://dx.doi.org/10.1016/j.actamat.2012.09.067

the SFs. Furthermore, structural information about the lattice location of solute atoms, which is very important to describe and model the Suzuki segregation, cannot be obtained from EDS microanalysis. Thus, direct imaging of the solute atom distribution along the SFs would be the key to an in-depth understanding of the Suzuki segregation and its effect on the mechanical properties of materials.

A previous study showed that SFs in cast Mg–Zn–Y alloys exhibited local solute enhancement [13] and thus may be well suited for studying Suzuki segregation. The strength of $Mg_{97}Zn_1Y_2$ can be increased to 600 MPa by rapid solidification processing, and its tensile strain to failure is up to 5% at room temperature, making these materials suitable in applications for lightweight structural materials [14–18]. Importantly, the strength of $Mg_{97}Zn_1Y_2$ at 300 °C is just slightly lower than that at room temperature [13]. This is different from the dramatic softening at elevated temperatures that commonly takes place in most metallic alloys. Long-period stacking ordered (LPSO) structures are believed to play an important role in strengthening Mg–Zn–Y alloys [13–15]. However, the superior strength at elevated temperatures cannot be simply attributed to the LPSO structures along grain boundaries. The Mg matrix must also play a role in the remarkable strength at elevated temperatures. Moreover, it is not just the solute providing increased lattice friction for dislocation motion because this effect decreases with increasing temperature. Therefore, there must be another mechanism at play during deformation within the Mg grains themselves that makes the dislocation motion difficult at elevated temperatures.

In the present work, we studied the atomic-scale microstructures and their evolution in the Mg matrix of an Mg–Zn–Y alloy upon plastic deformation at 300 °C. While deformation-induced nanometer-wide SFs with Suzuki segregation have been extensively observed, Suzuki segregation is confirmed herein at the atomic level for the first time. Models for different dislocation dissociation reactions are presented to explain the formation mechanisms of the different faulted structures we observe. The newly formed nanometer-wide SFs accompanied by Suzuki segregation, together with the SFs formed during growth, can effectively impede dislocation motion within the Mg grains, and thus play an important role in the superior strength at elevated temperatures.

2. Experiments

A $Mg_{97}Zn_1Y_2$ alloy was prepared using a vacuum melting furnace. Samples of size 4 mm × 4 mm × 8 mm were compressed to a strain of ~20.0% at a strain rate of $1.0 \times 10^{-3}\ s^{-1}$ at 300 °C, and then quenched into water to minimize thermo-driven microstructural evolution after the deformation. Specimens for microstructural investigations were cut in the direction perpendicular to the compression axis, mechanically polished, then ion milled.

A Nion UltraSTEM100 scanning transmission electron microscope (STEM) equipped with a fifth-order aberration corrector was used to characterize the atomic-scale structures of defects. High-resolution Z-contrast images were obtained using a high angle annular dark-field (HAADF) detector, which collects electrons that pass close to the atomic nucleus and, thus, scatter with intensities that approach the Z^2 dependence of Rutherford scattering [19]. It is thus possible to observe the atomic scale Zn/Y solute segregation in the Mg–Zn–Y alloy using the HAADF–STEM technique. The microscope was operated at 60 kV in order to reduce beam etching during atomic resolution imaging. HAADF observations were carried out using a half-angle range of 86–200 mrad, in order to eliminate the effect of strain contrast on images around dislocations [19]. The high-resolution images were processed using a double Gaussian filter [20].

3. Results and modeling

Fig. 1 shows Z-contrast images recorded from the Mg matrix in the as-cast (a) and deformed (b) samples. There are large planar defects in both samples, as shown by the long bright lines. These are growth SFs with Zn/Y segregation on basal planes according to high-resolution Z-contrast imaging, as shown in Fig. 2. Some nanometer-sized bright features that are parallel to the growth SFs appear in the deformed material, as indicated by arrows in Fig. 1b. This demonstrates that the deformation at 300 °C induces Zn/Y segregation on the nanometer scale, which will be investigated by high-resolution Z-contrast imaging, as shown below.

Fig. 2 shows a high-resolution Z-contrast image of a region containing several growth SFs in a Mg grain. The stacking sequence across all the SFs has the same order "...AB ABCA CA...", although there are two twin-related variants, as seen in the SFs marked "1" and "2". The middle "B" and "C" layers have a local face-centered cubic (fcc) environment, and they are much brighter than the neighboring "A" layers, showing higher concentration of Zn/Y in the two middle layers, which is a common characteristic of all growth SFs.

Fig. 3 shows a Thompson hexahedron for the hexagonal close packed (hcp) structure [21,22] that is convenient for the description of the characteristics, motion and dissociation of dislocations in Mg. Vectors ***AB***, ***BC*** and ***CA*** represent perfect "**a**" dislocations (Burgers vector, $\boldsymbol{b} = \frac{1}{3}\langle 11\bar{2}0\rangle$); vector ***ST*** is the perfect "**c**" dislocation ($\boldsymbol{b} = \langle 0001\rangle$); vectors ***SA/TB***, ***SB/TC*** and ***SC/TA*** (which are respectively the sum of vectors ***ST*** and ***AB***, or ***BC***, or ***CA***) are "**a** + **c**" perfect dislocations ($\boldsymbol{b} = \frac{1}{3}\langle 11\bar{2}3\rangle$). Other vectors, such as ***Aδ***, ***δS*** and ***AS***, represent partial dislocations with Burgers vectors of $\frac{1}{3}\langle 1\bar{1}00\rangle$, $\frac{1}{2}\langle 0001\rangle$ and $\frac{1}{6}\langle 2\bar{2}03\rangle$, respectively. Dissociation of 60° "**a**" dislocations, screw "**a**" dislocations, and "**a** + **c**" dislocations, as well as corresponding Suzuki segregation are studied here at the atomic level, and will be discussed in the following sections. All the high-resolution

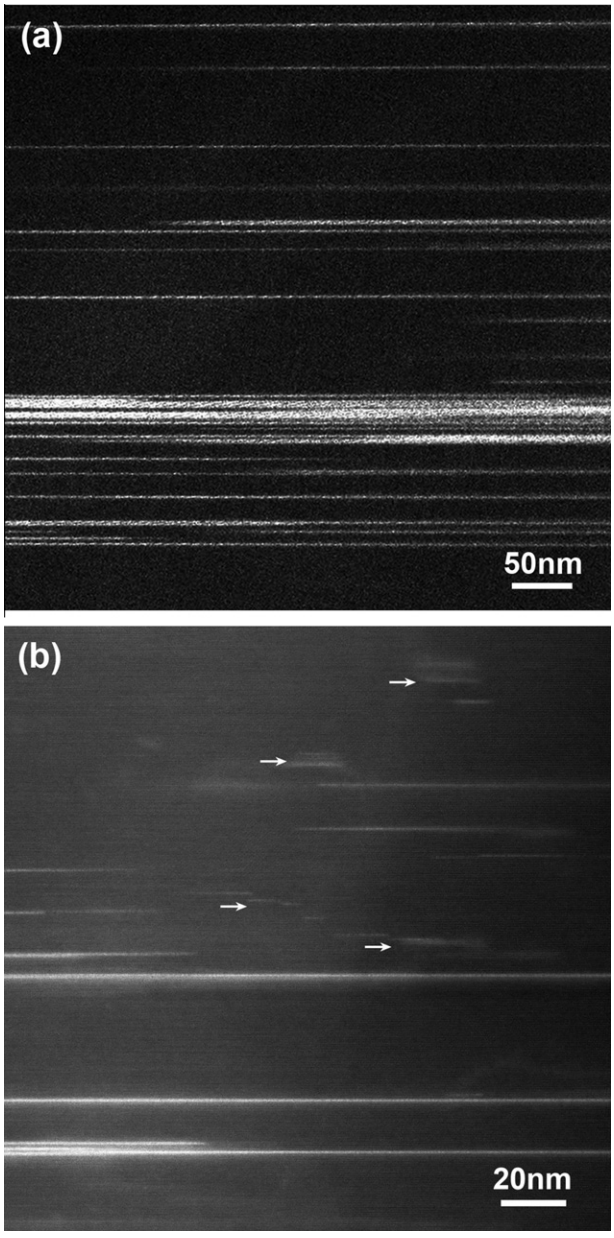

Fig. 1. Low magnification Z-contrast images showing planar defects in Mg grains, (a) as-cast, (b) deformed.

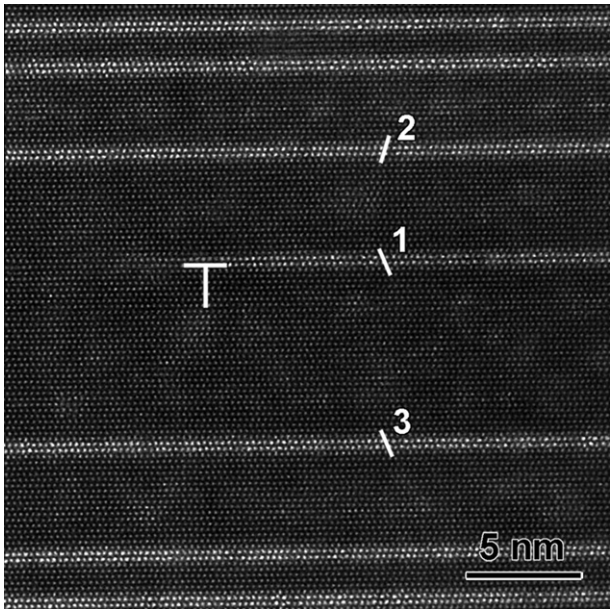

Fig. 2. High-resolution Z-contrast image showing planar defects with Zn/Y segregation within Mg grains in the as cast sample. "⊥" indicates a partial dislocation bounding one SF.

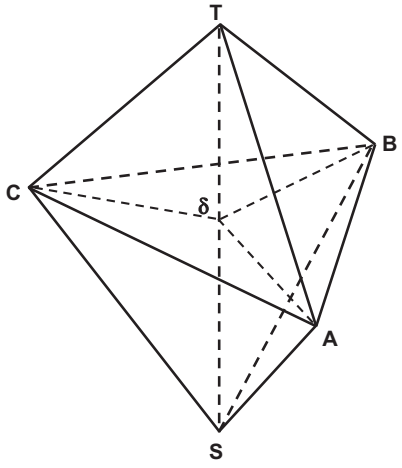

Fig. 3. Thompson hexahedron for dislocations in hcp structure. ABC represents the basal plane, and ST indicated the *c* axis of the hcp structure.

images in the present work are recorded along the zone axis parallel to vector ***AB***.

3.1. 60° "***a***" *dislocation*

Fig. 4a is a high-resolution Z-contrast image for one of the nanometer-sized bright features in the deformed sample. It has the same stacking sequence as the growth SFs, as shown by the short black line, indicating the formation of a deformation SF. The SF width (the distance between the two associated partials) is ~18 nm. Also the two middle layers are brighter due to higher concentration of Zn/Y, compared with the adjacent layers, as shown by the line intensity profile in Fig. 4b. But nanometer scale fluctuations of the in-plane Zn/Y distribution can be identified along the newly formed SF, which is different from uniform contrast observed along the growth SFs, as shown in Fig. 2. The closure failure of the Burgers vector surrounding the deformation SF indicates that it is associated with the dissociation of a 60° perfect "**a**" dislocation ($AC \rightarrow A\delta(30^{\circ}) + \delta C(90^{\circ})$ or $BC \rightarrow B\delta + \delta C$). The Shockley dislocations bounding the left and right ends of the SF are determined to be a 30° partial and a 90° partial, according to the observed magnitude of the corresponding Burgers vectors, as shown respectively in Fig. 4c and d.

3.2. Screw "***a***" *dislocation*

Fig. 5 shows a high-resolution Z-contrast image for another type of deformation SF. The SF width is ~7 nm.

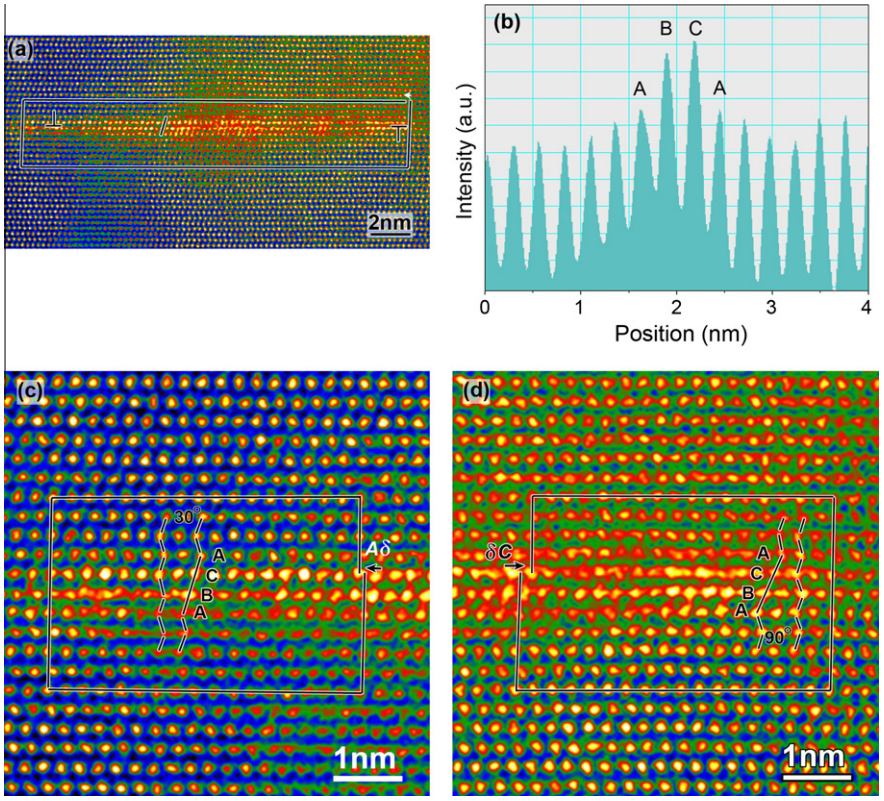

Fig. 4. (a) High-resolution Z-contrast image showing the dissociation of a 60° "**a**" dislocation and corresponding Suzuki segregation, (b) line profile crossing the SF demonstrating higher Zn/Y segregation in the middle planes "B" and "C" and (c, d) enlarged Z-contrast images showing the partial dislocations bonding the left and right side of the SF.

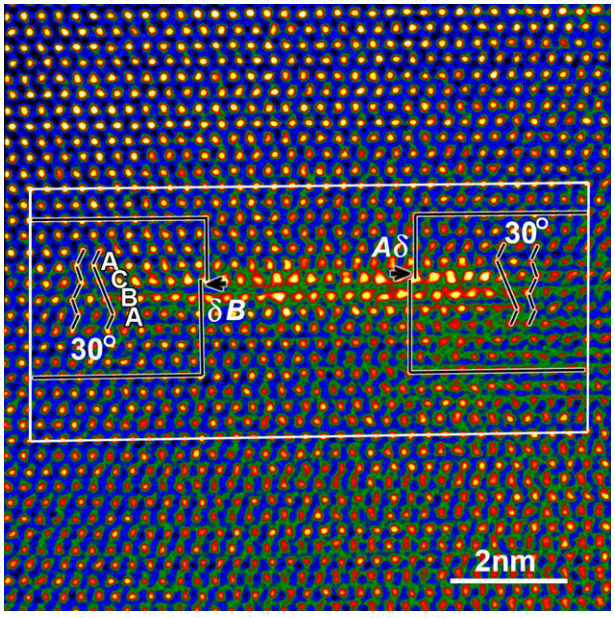

Fig. 5. High-resolution Z-contrast image showing the dissociation of a screw "**a**" dislocation and corresponding Suzuki segregation. The white lines form the Burgers circuit around the dissociated dislocation, showing no closure failure.

There is no closure failure for the total Burgers circuit, as shown by the white lines. Therefore, this deformation SF is a result of the dissociation of a screw "**a**" dislocation into two 30° partials ($AB \rightarrow A\delta(30^{\circ}) + \delta B(30^{\circ})$), as indicated by the closure failure of the Burgers circuits for the two partials. The higher intensities of the two middle basal planes of the faulted region demonstrate the occurrence of Zn/Y segregation along the SF.

3.3. "***a*** + ***c***" *dislocations*

"**a** + **c**" dislocations have been observed in various Mg alloys, and they play an important role in the deformation behavior and mechanical properties of Mg alloys [23–25]. Fig. 6 shows high-resolution Z-contrast images for a SF with a width of ~16 nm that is the result of the dissociation of an "**a** + **c**" dislocation, as indicated by closure failure of the Burgers circuit in Fig. 6a. And the "**a**" component of this dislocation has a 60° character, ***AC*** or ***BC***. The two circles indicate the position of the partial dislocations. It can be seen that there is considerably less segregation of Zn/Y to this SF compared with that seen with the SFs shown in Figs. 4 and 5, although there are some brighter columns within this faulted structure, as indicated by arrows in Fig. 6a. More interestingly, this is a three-layer faulted structure with a stacking sequence of "…AB ABC BC…", rather than the four-layer faults shown in Figs. 4 or 5, as seen from the enlarged images for the two ends of the SF in Fig. 6b and c. The stacking sequence of this three-layer faulted structure is the same as an intrinsic growth SF [21].

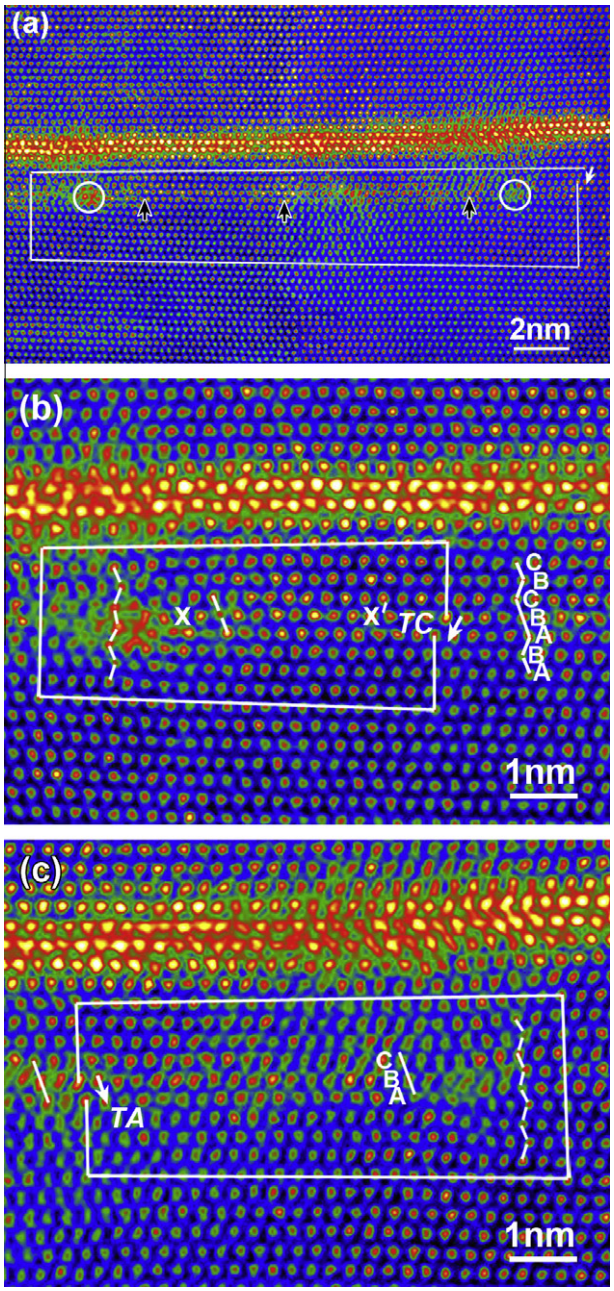

Fig. 6. (a) High-resolution Z-contrast image showing the dissociation of an "**a** + **c**" dislocation, Suzuki segregation and the formation of a three-layer faulted structure, (b,c) enlarged images for both ends of the SF. The "**a**" component is a 60° dislocation.

The Burgers vectors for the partial dislocations bounding the left (Fig. 6b) and right (Fig. 6c) ends of the SF are determined to be ***TC*** and ***TA*** (or ***TB***), respectively. It is seen that $TC = T\delta\left(\frac{1}{2}\langle 0001\rangle\right) + \delta C(90^\circ)$, $TA = T\delta + \delta A(30^\circ) = \delta S\left(\frac{1}{2}\langle 0001\rangle\right) + \delta A$, according to the Thompson hexahedron shown in Fig. 3. However, $TC + TA = TS + \delta C + \delta A$, which is not equivalent to the Burgers vector of $TS + AC = TA/SC$, for an "**a** + **c**" dislocation, since $\delta C + \delta A = B\delta \neq AC$. This is not consistent with the Burgers circuit around the SF in Fig. 6a. The discrepancy implies that other atomic processes must be involved in the dissociation of the "**a** + **c**" dislocation and the following movements of the partial dislocations, and they have modified the partial dislocations on both ends of the SF.

Fig. 7 shows high-resolution Z-contrast images from a five-layer faulted structure with a stacking sequence of "...AB ABCAB AB...". The intensities of atomic columns indicate that there is Zn/Y segregation within all the five basal layers of the fault, as shown by the line intensity profile across the faulted structure in Fig. 7b. The intensity variation along the basal planes is attributed to in-plane concentration fluctuation of solute atoms, which is similar to the cases shown in Figs. 4 and 6. The closure failure of the Burger circuit shows that the faulted structure is related to a perfect "**c**" edge dislocation, as indicated by the arrow in Fig. 7a. The "...AB ABCAB AB..." stacking is known as an extrinsic SF in the hcp structure and can be simply achieved by inserting a section of "C" plane into the hcp lattice [21,22]. But the Burgers circuit surrounding such a SF will not show a closure failure equivalent to a perfect "**c**" dislocation like that shown in Fig. 7a. Moreover, a "**c**" dislocation dissociates into two $\frac{1}{2}\langle 0001\rangle$ partials that on their own cannot produce the observed five-layer faulted structure. It can be concluded that the dislocation associated with this five-layer faulted structure is not a simple "**c**" dislocation and must contain a screw component parallel to the viewing direction. Therefore, the five-layer fault is probably the result of the dissociation of an "**a** + **c**" dislocation.

Fig. 7c and d shows enlarged images for both ends of the five-layer faulted structure. The closure failure of both the Burgers circuits is $\frac{c}{2}$, matching exactly that for an extrinsic SF generated by inserting an extra "C" basal plane into the hcp lattice. Fig. 7c and d demonstrates that the "**c**" edge component dissociated into two $\frac{c}{2}$ partials, and they climbed in opposite directions. Interestingly, no partial dislocations due to dissociation of the screw "**a**" component of the "**a** + **c**" dislocation can be identified on the basal plane, according to the Burgers circuits in Fig. 7c and d. However, the screw "**a**" component must dissociate into two 30° partial dislocations that have been involved in the formation of the five-layer fault, since (i) the glide of a perfect screw dislocation on the basal plane does not change the observed stacking sequence, and (ii) the "**c**" component itself cannot produce the five-layer fault. The lack of dissociated 30° partial dislocations implies that processes other than climb of $\frac{c}{2}$ partial dislocations and glide of 30° partial dislocations must take place accompanying the formation of the five-layer faulted structure, and such processes annihilate or shroud the 30° partials. The complex cases shown in Figs. 6 and 7 will be modeled in the following based on the principles of dislocation dissociation, as shown in Figs. 8 and 9, respectively.

It is seen that there is difference in the concentration of Zn/Y segregation among the observed deformation SFs, as shown in Figs. 4–7. For example, the amount of Zn/Y segregation within the three-layer faulted structure (Fig. 6) is obviously less than those of other SFs (Figs. 4, 5 and 7).

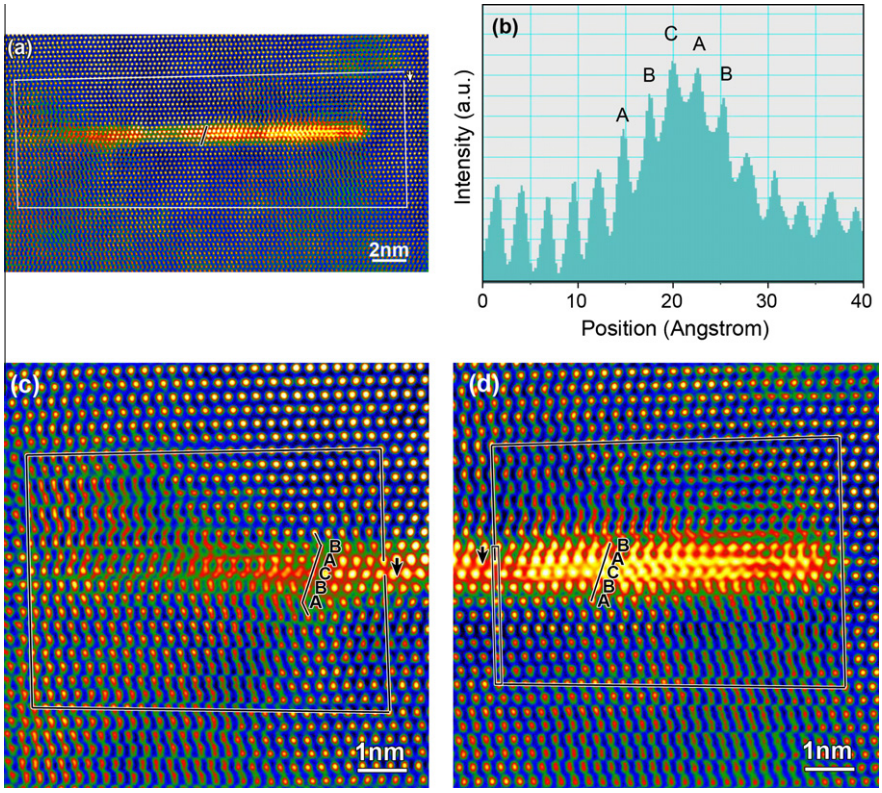

Fig. 7. (a) High-resolution Z-contrast image showing the dissociation of another **a** + **c** dislocation, Suzuki segregation and the formation of a five-layer faulted structure, (b) line profile across the SF showing Zn/Y segregation in five successive basal layers, (c,d) enlarged images for both ends of the SF. The "**a**" component is a screw dislocation.

Also, there are changes in Zn/Y concentration from one end to the other end within the five-layer faulted structure (Fig. 7). The variation of Zn/Y concentration should be a result of fluctuation in solute concentration within the Mg matrix, since the surrounding Mg matrix is the supplier of solute atoms.

3.4. Modeling dislocation dissociation and partial dislocation motion

For simplicity we will describe the dislocation dissociation using a pure Mg hcp structure in this section, without considering the associated Zn/Y segregation. The local enhancement of solute atoms, as shown in Figs. 4–7, is direct atomic-scale evidence for the occurrence of Suzuki segregation during the deformation at 300 °C, which will be discussed in Section 4.1.

3.4.1. "*a*" dislocation

A perfect "**a**" dislocation can dissociate into two Shockley partials, like $AC(60^\circ) \rightarrow A\delta(30^\circ) + \delta C(90^\circ)$ or $AB(screw) \rightarrow A\delta(30^\circ) + \delta B(30^\circ)$ for a 60° or a screw dislocation, as shown respectively in Figs. 4 and 5. Partials $\delta C(90^\circ)$ and $\delta B(30^\circ)$, which are respectively opposite to $C\delta$ and $B\delta$, are not allowed to move on the same slip plane of the partial $A\delta(30^\circ)$, since such glide would produce "A-A" type stacking which violates the close packed hcp structure. Therefore, the two partials have to glide on two adjacent basal planes, as demonstrated in Figs. 4 and 5.

3.4.2. "*a* + *c*" dislocations

In the case of the dissociation of "**a** + **c**" dislocations, the $\frac{c}{2}$ partials are required to climb in order to catch up with the Shockley partials moving on the basal planes. Climb of dislocations requires mass transport by diffusion, which is normally slower than slip induced by shear. Thus the Shockley partials are expected to start to glide prior to the climb of the $\frac{c}{2}$ partials; and the moving Shockley partials can act as pipe diffusion pathways to support the climb of the following $\frac{c}{2}$ partial.

Fig. 8 shows atomic models for the dissociation of the "**a** + **c**" dislocation and the formation of the three-layer fault structure shown in Fig. 6. Firstly, the 60° "**a**" dislocation dissociates into a 30° partial $A\delta$ and a 90° partial δC. Secondly, glide of the 30°/90° partial shifts the part below/above the dashed line toward the left/right, resulting in the formation of a deformation SF (from step (i_L) to (ii_L), and (i_R) to (ii_R)). Thirdly, the two dissociated $\frac{c}{2}$ partials locating just above the SF start to climb. The left $\frac{c}{2}$ partial undergoes the so-called negative climb, which means inserting a "C" plane, as shown by step (iii_L) in Fig. 8. However, a local "C-C" stacking will be produced by inserting a "C" plane, which is not allowed. The right $\frac{c}{2}$ partial undergoes positive climb by means of atoms diffusing away from the

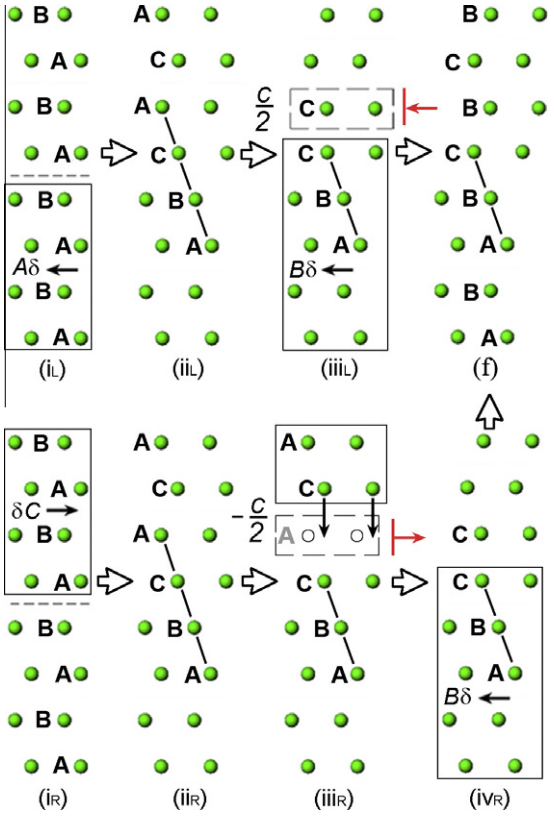

Fig. 8. Formation mechanisms for the three-layer faulted structure. The red symbols of "⊥" with an arrow represent the $\frac{c}{2}$ partial dislocations, and the arrow indicates their corresponding climb direction. (For interpretation of the references to color in this figure legend, the reader is referred to the web version of this article.)

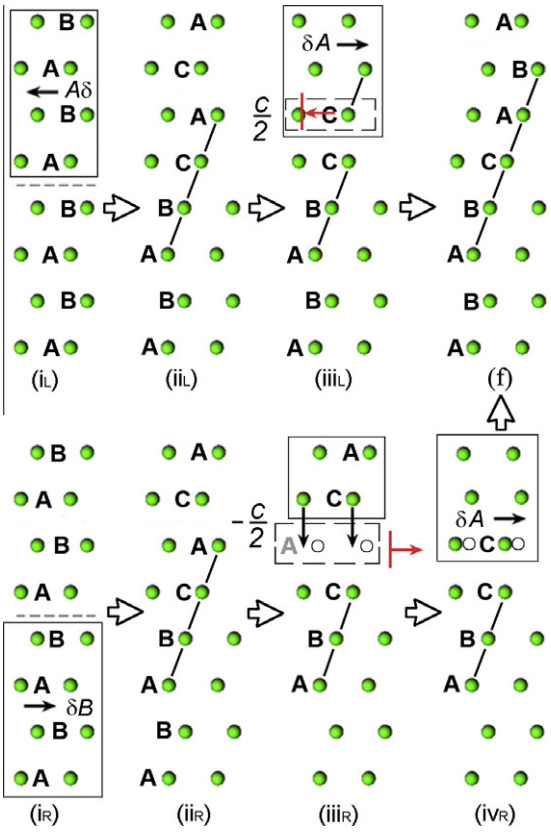

Fig. 9. Formation mechanisms for the five-layer faulted structure. The red symbols of "⊥" with an arrow represent the $\frac{c}{2}$ partial dislocations, and the arrow indicates their corresponding climb direction. (For interpretation of the references to color in this figure legend, the reader is referred to the web version of this article.)

"A" plane, which also results in the appearance of "C-C" stacking, as shown by (iii_R) and (iv_R) in Fig. 8. An extra shear between the two "C" planes is required in order to remove the "C-C" stacking. If the lower part containing the lower "C" plane, as indicated by the rectangular boxes in (iii_L) and (iv_R) of Fig. 8, is sheared by $B\delta$ relative to the upper part, it will lead to the "…AB ABC BC…" stacking sequence, as shown by (f) in Fig. 8. This is the same stacking sequence as observed in the three-layer faulted structure shown in Fig. 6. The final Burgers vectors for the partials bonding the left and right ends of the three-layer faulted structure can be determined to be Eqs. (1a) and (1b), respectively:

$$T\delta + A\delta(30^\circ) + B\delta(30^\circ) = T\delta + \delta C(90^\circ) = TC \quad (1a)$$

$$\delta S + \delta C(90^\circ) - B\delta(30^\circ) = T\delta + \delta A(30^\circ) = TA \quad (1b)$$

They are consistent with the Burgers circuits shown in Fig. 6b and c. The two Shockley partials cannot exchange their position for the case shown in Fig. 6, according to Eq. (1). It is seen that the 30° and 90° Shockley partials $A\delta$ and δC are shrouded by the extra shear of $B\delta$. Therefore, the discrepancy between the whole Burgers circuit and the sum of the two partials surrounding the end regions of the fault is attributed to the extra shear of $B\delta$ to remove the "C-C" stacking associated with the climb of the $\frac{c}{2}$ partials.

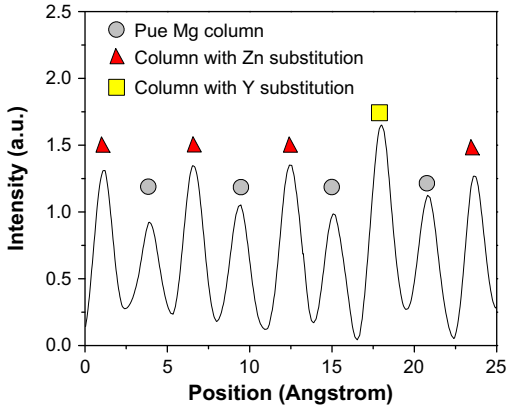

Fig. 10. Line profile showing the intensity variation of atomic columns and the corresponding substitutions.

Fig. 9 shows atomic models for the dissociation of the "**a** + **c**" dislocation and the formation of the five-layer faulted structure shown in Fig. 7. Here we assume that the "**a**" component of the "**a** + **c**" dislocation is AB, and it dissociates as $AB(screw) \rightarrow A\delta(30^\circ) + \delta B(30^\circ)$, as shown by ($i_L$) and ($i_R$) in Fig. 9. There are two equivalent ways to produce the final five-layer faulted structure through the dissociation of an "**a** + **c**" dislocation. (i) The upper part

containing the upper "C" plane is sheared by δA, in order to accommodate the climb of the two $\frac{c}{2}$ partials, and finally produce a five-layer faulted structure shown by (f) in Fig. 9. The final Burgers vectors for the dislocation bonding the left and right ends of the five-layer faulted structure can be described by Eqs. (2a) and (2b), respectively:

$$T\delta + A\delta + \delta A = T\delta\left(\frac{1}{2}\langle 0001\rangle\right) \tag{2a}$$

$$\delta S + \delta B - \delta A = \delta S\left(\frac{1}{2}\langle 0001\rangle\right) + AB(screw) \tag{2b}$$

(ii) If the upper part is sheared by δB, the dislocation bonding the left and right ends of the five-layer faulted structure will be Eqs. (3a) and (3b), respectively:

$$T\delta + A\delta + \delta B = T\delta\left(\frac{1}{2}\langle 0001\rangle\right) + AB(screw) \tag{3a}$$

$$\delta S + \delta B - \delta B = \delta S\left(\frac{1}{2}\langle 0001\rangle\right) \tag{3b}$$

They both are consistent with the Burgers circuits in Fig. 7c and d. Therefore, there should be a screw dislocation on one side of the five-layer faulted structure. But its position cannot be determined based on the high-resolution Z-contrast images. The "...ABCAB..." extrinsic SF can be generated by simply inserting a basal plane into the hcp lattice, which requires a shear equivalent to the glide of a Shockley partial in order to remove the "A-A" or "B-B" stacking. The Burgers circuit surrounding the ends of the final SF will show a closure failure with a component for the Shockley partial. Therefore, the five-layer faulted structure shown in Fig. 7 is the result of the dissociation of an "$\mathbf{a}+\mathbf{c}$" dislocation, instead of simply inserting a basal plane into the Mg matrix.

4. Discussion

4.1. Suzuki segregation

Suzuki segregation is believed to have a strong influence on the mechanical properties of alloys. For example, the strength of cold-rolled Co–Ni-based superalloys is believed to be further increased by aging at intermediate temperatures due to the Suzuki segregation, although no direct evidence was obtained by microanalysis [4]. In addition, phenomena such as serrated flow, positive temperature dependence of strength, dynamic strain aging (abnormal strain rate dependences of flow stress) and deformation twinning in alloys are often attributed to the interactions between dislocations and solute atoms in the form of Cottrell atmospheres and/or Suzuki atmospheres [3–6]. The appearance of SFs (i) in samples plastically deformed at elevated temperatures, or (ii) in aged samples after cold deformation, is considered to be evidence for Suzuki segregation [4–6,9–12]. However, Suzuki segregation has not been verified directly on the atomic level.

As shown in Figs. 4 and 5, the atomic columns within the middle two planes "B" and "C" having a local fcc environment show higher concentration of Zn/Y according to their higher intensities, compared with other basal planes with hcp environment, including the two "A" planes of the four-layer "ABCA" structure. Those atomic columns indicated by arrows in the "B" and "C" planes are obviously enhanced by Zn/Y segregation, compared with others within the three-layer faulted structure in Fig. 6. All the five "ABCAB" planes of the five-layer faulted structure have higher concentration of Zn/Y, according to the intensity line profile shown in Fig. 7b. Those results demonstrate directly the occurrence of Suzuki segregation of solute atoms to SFs on the atomic level.

Fig. 10 shows the variation of intensities for atomic columns between X and X′ in Fig. 6b. The peak maxima are normalized by assuming that those weaker atomic columns are composed of pure Mg atoms, and setting their intensities to 1.0 ± 0.1. The focus depth is evaluated to be ~4 nm for our experimental settings. The theoretical normalized intensity for an atomic column of 4 nm long with one Zn or Y substitution atom is thus ~1.38 or 1.68, respectively, according to the Z^2 law. Therefore, the intensity line profile indicates that there are four atomic columns with Zn substitution and one with Y substitution, and they distribute alternately with pure Mg columns. There is higher Suzuki segregation for the other three cases shown in Figs. 4, 5 and 7, according to the corresponding higher intensities of more atomic columns. Zhu et al. [26] observed a kind of intrinsic SF in an annealed Mg–Zn–Y-based alloy, but they did not detect the Suzuki segregation along the SF using the HAADF–STEM technique. They thought that it was because their samples were too thick. Other previous results on the Suzuki segregation were based on EDX measurements with nanometer spatial resolution, and no direct identification of solute atoms has yet been achieved [4,5,11,12]. Furthermore, the signals for the solute elements are rather weak and noisy in the reported EDS spectra. For example, Koizumi et al. [12] reported that the low signal-to-noise ratio made it impossible to obtain any data on solute segregation across SFs in their Co–Ni-based superalloys using EDS. Therefore, our experimental observations confirm the Suzuki segregation directly, and provide the distribution of solute atoms on the atomic level for the first time. The Suzuki segregation to the newly formed nanometer-wide SFs hinders their further motion, and can also serve as nanometer-sized blocking centers, acting like precipitates or GP zones, for other dislocations. This is believed to be responsible, at least partly, for the superior strength at elevated temperatures of the Mg–Zn–Y alloys.

4.2. SF energy and resolved shear stress on Shockley partials

The deformation-induced SFs in our samples are 7–18 nm wide, as shown in Figs. 4–7. The SF energy, γ, is thus calculated to be in the range of 4.0–10.3 mJ m^{-2}, based on the following equation [27]:

$$\gamma = \frac{\mu b^2}{8\pi d}\frac{2-v}{1-v}\left(1-\frac{2v}{2-v}\cos 2\theta\right) \quad (4)$$

where μ and v are the shear modulus (17 GPa) and Poisson's ratio (0.35) for Mg, b is the magnitude of the Burgers vector of the Shockley partials (0.186 nm), d is the measured width of the SF, θ is the angle between the Burgers vectors of the two partials. The SF energy for pure Mg is in the range of 30–80 mJ m^{-2} according to experimental measurements and first-principles calculations [28–32]. First-principles calculations also showed that ~2 at.% addition of Zn could decrease the Mg SF energy to 18.8 mJ m^{-2}, while Y would increase it to 113.2 mJ m^{-2} [30]. The SF energy for the present Mg–Zn–Y alloy (4.0–10.3 mJ m^{-2}) is considerably lower than that for pure Mg (30–80 mJ m^{-2}) [25–29], and Mg alloyed with about 2 at.% addition of Zn (18.8 mJ m^{-2}) [30]. It should be pointed out that our samples were deformed at 300 °C. The estimated SF energy should be lower than that deduced from samples deformed at room temperature and first-principles calculations at −273 °C. Zhu et al.'s [26] results showed that addition of Zr to Mg–Zn–Y alloy reduced the SFE alloy further to 0.9–1.8 mJ m^{-2}.

The resolved shear stress (τ) required to move the partial dislocation can be described by [33]:

$$\tau \geq \frac{\gamma}{b} + \tau_p \quad (5)$$

where $\tau_p = \frac{2\mu}{K}\exp\left(-\frac{2\pi a}{Kb}\right)$ is the lattice resistance, in which K is a constant and a is the distance between two adjacent slip planes (~0.26 nm for Mg). It is thus deduced that the critical value for τ is in the range of 26.5–60.4 MPa, in order to keep the partials moving in the $Mg_{97}Zn_1Y_2$ alloy. The yield and peak flow stresses of our $Mg_{97}Zn_1Y_2$ alloy are 90 and 190 MPa, respectively [13]. Therefore, the deduced critical resolved shear stress on the Shockley partials is in a reasonable range, considering the Schmid factors for dislocations within each individual Mg grain.

4.3. Co-segregation of Zn and Y

Segregation of Zn from the hcp matrix to the SFs is expected to lower the system energy, since the addition of Zn decreases the SF energy of Mg [30]. Therefore, the local Zn enhancement is reasonably attributed to the chemical interaction between Zn and the SFs [2]. However, there is also Y segregation along the SFs in the present Mg–Zn–Y alloy, which cannot be rationalized through chemical interaction, since the addition of Y increases the SF energy of Mg [30]. However, a Zn atom is smaller than a Mg atom, while an Y atom is larger than a Mg atom. The lattice distortion originating from segregation of Zn atoms to the SFs can therefore attract Y atoms in the vicinity to diffuse to the SFs in order to lower the local strain energy. On the other hand, if a SF happens to pass some Y atoms, the lattice dilatation surrounding those Y atoms would provide extra driving force for the diffusion of Zn atoms in the vicinity of the SFs, in addition to the chemical interactions between the SFs and Zn atoms. Therefore, the co-segregation of Zn and Y along the SFs is the combined result of chemical and size effects, and the Suzuki segregation of Zn atoms promotes the segregation of Y atoms toward the SFs, and vice versa. The co-segregation of Zn and Y to SFs is thus more energetically favorable than having only Zn segregation along the SFs in the Mg–Zn–Y system.

5. Conclusions

- Three types of SF with nanometer width were formed in the $Mg_{97}Zn_1Y_2$ alloy upon deformation at 300 °C. Dissociation of "**a**" dislocations produced intrinsic (deformation) SFs with the stacking sequence of "...AB ABCA CA...". Dissociation of "**a** + **c**" dislocations may produce three-layer or five-layer faulted structures with respectively the stacking sequence of "...AB ABC BC" or "...ABC ABCAB AB..." depending on the character of the "**a**" component and motion of the partials.
- Atomic resolution Z-contrast imaging demonstrates the occurrence of the Suzuki segregation of Zn and Y to the SFs, and shows the distribution of solute atoms with atomic resolution. The solute concentration is higher within atomic columns having local fcc environments.
- The co-segregation of Zn and Y to the SFs is the result of chemical interaction between Zn atoms and the SFs and strain minimization arising from Zn and Y atomic size differences. The SF energy is estimated to be in the range of 4.0–10.3 mJ m^{-2}, as determined from the measured widths of SFs. This SF energy value for the Mg–Zn–Y alloy is much lower than that for pure Mg and binary Mg alloys of Mg–Zn and Mg–Y, but higher than that of a Mg–Zn–Y–Zr alloy.

Acknowledgements

ZQY, MFC and SJP are supported by the US Department of Energy, Office of Basic Energy Sciences, Materials Sciences and Engineering Division. ZQY thanks the NSFC (51171189), the MoST of China (2009BC623705) and the NSF of Liaoning Province for support. Instrument access was provided by Oak Ridge National Laboratory's ShaRE User Facility, which is sponsored by the Scientific User Facilities Division, Office of Basic Energy Sciences, US Department of Energy.

References

[1] Cottrell AH, Bilby BA. Proc Phys Soc Lond Sec A 1949;62:49.
[2] Suzuki H. Sci Rep Res Inst Tohoku Univ A 1952;4:455.
[3] Cui CY, Gu YF, Yuan Y, Harada H. Scr Mater 2011;64:502.
[4] Koizumi Y, Nukaya T, Suzuki S, Kurosu S, Li YP, Matsumoto H, et al. Acta Mater 2012;60:2901.

[5] Han GW, Jones IP, Smallman RE. Acta Mater 2003;51:2731.
[6] Rao KBS, Castelli MG, Ellis JR. Scr Metall Mater 1995;33:1005.
[7] Blavette D, Cadel E, Fraczkiewicz A, Menand A. Science 1999;286:2317.
[8] Wilde J, Cerezo A, Smith GDW. Scr Mater 2000;43:39.
[9] Gallagher PCJ. Metall Trans 1970;1:2429.
[10] Remy L, Pineau A, Thomas B. Mater Sci Eng 1978;36:47.
[11] Mendis BG, Jones IP, Smallman RE. J Electron Micros 2004;53:311.
[12] Kamino T, Ueki Y, Hamajima H, Sasaki K, Kuroda K, Saka H. Philos Mag Lett 1992;66:27.
[13] Shao XH, Yang ZQ, Ma XL. Acta Mater 2010;58:4760.
[14] Inoue A, Kawamura Y, Matsushita M, Hayashi K, Koike J. J Mater Res 2001;16:1894.
[15] Itoi T, Takahashi K, Moriyama H, Hirohashi M. Scr Mater 2008;59:1155.
[16] Graces G, Onorbe E, Dobes F, Perez P, Antoranz JM, Adeva P. Mater Sci Eng A 2012;539:48.
[17] Yokobayashi H, Kishida K, Inui H, Yamasaki M, Kawamra Y. Acta Mater 2011;58:7287.
[18] Shao XH, Yang ZQ, You JH, Qiu KQ, Ma XL. J Alloys Compd 2011;509:7221.
[19] Pennycook SJ. Z-contrast STEM for materials science. Ultramicroscopy 1989;30:58.
[20] Krivanek OL, Chisholm MF, Nicolosi V, Pennycook TJ, Corbin GT, Dellby N, et al. Nature 2010;464:571.
[21] Hirth JP, Lothe J. Theory of dislocations. New York: Wiley; 1982.
[22] Hull D. Introduction to dislocations. Oxford: Pergamon Press; 1975.
[23] Matsuda M, Ando S, Nishida M. Mater Trans 2005;46:361.
[24] Galiyev A, Kaibyshev R, Gottstein G. Acta Mater 2001;49:1199.
[25] Fu PH, Pen LM, Nie JF, Jiang HY, Ma L, Bourgeois L. Mater Sci Forum 2011;690:230.
[26] Zhu YM, Morton AJ, Weyland M, Nie JF. Acta Mater 2010;58:464.
[27] Read Jr WT. Dislocations in crystals. Boston: Butterworth-Heinemann; 1953.
[28] Sastry DK, Prasad YVRK, Vasu KI. Scr Metall 1969;3:927.
[29] Couret A, Caillard D. Acta Metall 1985;33:1455.
[30] Datta A, Waghmare UV, Ramamurty U. Acta Mater 2008;56:2531.
[31] Chetty N, Weinert M. Phys Rev B 1997;56:10844.
[32] Smith AE. Surf Sci 2007;601:5762.
[33] Lagerlof KPD, Castaing J, Pirouz P, Heuer AH. Philos Mag A 2002;82:2841.